Journal of Applied Physics

RESEARCH ARTICLE | OCTOBER 01 2025

Study of the temperature dependent trap-dominated conduction in GeSe and $GeSe_2$ Ovonic threshold switching selectors

Jonas Keukelier ; Seppe Van Dyck ; Wouter Devulder ; Karl Opsomer; Christophe Detavernier

Check for updates

J. Appl. Phys. 138, 135101 (2025)
https://doi.org/10.1063/5.0279599

View Online
Export Citation

Articles You May Be Interested In

Tuning of the thermal stability and ovonic threshold switching properties of GeSe with metallic and non-metallic alloying elements

J. Appl. Phys. (October 2021)

Understanding ovonic threshold switching of GeSe chalcogenide materials using electrical methodologies for extracting density of states

Appl. Phys. Lett. (August 2023)

First-principles prediction of the native filament:dielectric interfaces for the possible filamentary switching mechanism in chalcogenide selector devices

J. Appl. Phys. (January 2020)

16 July 2026 09:01:14

Zurich Instruments
Freedom to Innovate.
The New VHFLI 200 MHz Lock-in Amplifier.
Orchestrate pulses, triggers, and acquisition as the hub of your experiment.
Discover more – run every signal analysis tool, simultaneously.
Order now

AIP Publishing

Journal of Applied Physics ARTICLE pubs.aip.org/aip/jap

Study of the temperature dependent trap-dominated conduction in GeSe and $GeSe_2$ Ovonic threshold switching selectors

Cite as: J. Appl. Phys. **138**, 135101 (2025); doi: 10.1063/5.0279599
Submitted: 7 May 2025 · Accepted: 10 September 2025 ·
Published Online: 1 October 2025

View Online Export Citation CrossMark

Jonas Keukelier,[1,a)] Seppe Van Dyck,[1] Wouter Devulder,[2] Karl Opsomer,[2] and Christophe Detavernier[1]

AFFILIATIONS

[1]Department of Solid State Sciences, Ghent University, Krijgslaan 281 (S1), 9000 Gent, Belgium
[2]Interuniversity Micro Electronics Center (IMEC), Kapeldreef 75, B-3001 Leuven, Belgium

[a)]**Author to whom correspondence should be addressed:** jonas.keukelier@ugent.be

ABSTRACT

The highly non-linear current–voltage characteristics of Ovonic threshold switching selectors make them a key component in novel 3D crossbar memory architectures. The sub-threshold conduction and switching mechanism have long been a point of debate but it is generally accepted that they are trap-assisted in nature. In this paper, we study the sub-threshold conduction of both pristine and switched amorphous GeSe and $GeSe_2$ devices across a wide temperature range spanning from up to 353 K down to 133 K. By applying a simple Poole–Frenkel model, insight can be gained into the average trap depth and concentration and how these are affected by temperature, composition, and layer thickness. It is found that the average trap depth is temperature dependent, suggesting a distribution of traps in the mobility gap with only very shallow traps contributing to the current at low temperatures. GeSe layers tend to have a significantly larger amount of traps than the $GeSe_2$ layers, in line with the hypothesis that wrongly coordinated Ge bonds are the dominant source of trap states. For thinner films, there are larger deviations from the simple Poole–Frenkel model for conduction, indicating an increasingly important effect of the interface barriers as the layer thickness decreases. After first-fire switching, the sub-threshold conduction changes drastically. The simple Poole–Frenkel model can still be applied, but quantitative information on the number of traps can no longer be reliably obtained.

© 2025 Author(s). All article content, except where otherwise noted, is licensed under a Creative Commons Attribution-NonCommercial 4.0 International (CC BY-NC) license (https://creativecommons.org/licenses/by-nc/4.0/). https://doi.org/10.1063/5.0279599

16 July 2026 09:01:14

I. INTRODUCTION

A selector is a component in novel memory architectures that serves to limit unwanted leakage currents through non-selected memory cells.[1] This is typically achieved by the selector component either exhibiting a highly non-linear current–voltage (IV) characteristic (i.e., a regular diode operated in the forward regime) or exhibiting a threshold voltage below which the device is highly resistive and above which the device becomes highly conductive.[2] Selectors based on Ovonic Threshold Switching (OTS) exhibit both of these features, which has already enabled their usage in emerging memory applications.[3] The functional material in these OTS devices is typically an amorphous chalcogenide, a compound containing S, Se, or Te. By better understanding the electrical properties of these materials and how they relate to other material properties, advancement in their application can be sped up considerably. In this paper, we study the sub-threshold conduction, i.e., the high-resistive state (HRS) of unalloyed, binary GeSe and $GeSe_2$ thin films incorporated into simple test structures. By using current–voltage measurements at varying temperatures, referred to as IV(T)s, insight can be gained into the dominant conduction mechanisms at work. While some studies of the IV(T) behavior of Ge containing thin film chalcogenides have already been performed on selector type devices, only rarely is the temperature regime expanded to below room temperature.[4–8] In this paper, we extend the IV(T) analysis to below room temperature in an effort to further elucidate the conduction mechanisms at work.

Previous publications have focused on the ambient electronic and material properties.[9–11] Compared to other OTS selector candidate materials, binary GeSe and $GeSe_2$ compounds tend to exhibit undesirably higher threshold voltages and require alloying

© Author(s) 2025

with elements such as N, C, Sb, As, Si, Te, or others to tune the OTS performance parameters to suitable levels, often resulting in a quaternary or even quinary switching layer. We have chosen to keep the material system simple as the primary purpose of this study was not to find a particularly optimal composition but rather to better understand the conduction mechanisms in GeSe-based chalcogenides in general. A binary material system can also be more easily deposited in a highly reproducible fashion, which allows for a more faithful comparison of results between samples. Finally, these binary systems had already been extensively researched in previous publications. Prior to the IV(T) analysis, the same material and ambient electrical characterization was performed again to ensure the quality and reproducibility of the results.

II. THE POOLE–FRENKEL CONDUCTION MECHANISM

While the exact mechanism of the volatile switching mechanism of chalcogenides is still a matter of discussion, it is generally agreed that the sub-threshold conduction is trap assisted in nature.[12,13] Poole–Frenkel (PF) conduction describes the conduction through an insulating or semiconducting material by means of emission of trapped charge carriers. These traps are considered neutral when filled and positive when empty, resulting in a coulomb potential type well. Trapped carriers can be excited to the conduction band by thermal energy after which they can move freely. However, if a sufficiently large electric field is present, the energy barrier that the trapped charge carriers need to overcome is reduced.[14] A schematic representation of this effect is given in Fig. 1. The PF effect is similar to Schottky emission over a metal–insulator interface with the fundamental difference that in PF conduction the positive charge is static, whereas in Schottky emission it is mobile. This results in a barrier lowering effect that is twice as large for PF conduction.[15] The PF current density can be mathematically modeled in the simplest form by the following formula, assuming a single trap level and that the traps are far enough apart

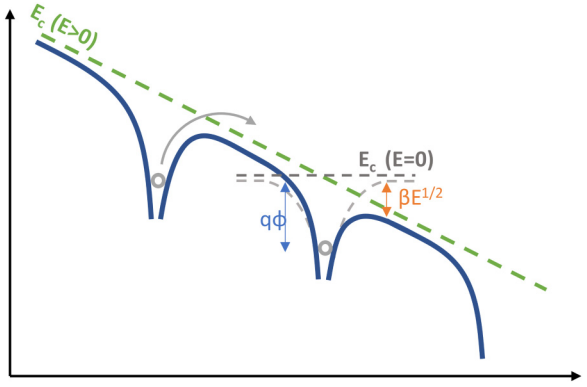

FIG. 1. Schematic energy band diagram of PF conduction. The barrier the charge carriers must overcome to reach the conduction band is reduced when an electric field F is applied compared to the situation when no field is present.

such that they do not influence each other,

$$J = q\mu N_c E \cdot \exp\left(-\frac{q\phi - \beta\sqrt{E}}{kT}\right) \quad (1)$$

where q is the elementary charge, μ is the charge mobility, $q\phi$ is the trap depth, N_c is the concentration of trap states in the bandgap, and the PF factor $\beta = \sqrt{\frac{q^3}{\pi\epsilon_r\epsilon_0}}$, which contains only material constants.[4,14,16–18] Other, more complicated descriptions exist that try to take into account various effects such as a three-dimensional description, e.g., Hartke's equation[19] or account for inter-trap interactions.[12] Additionally, some studies report different dependencies of the pre-exponential factor on the electrical field.[16,20,21] Such deviations are attributed to a range of effects such as charge re-trapping by nearest neighbors or after a constant drift time, field-dependent mobility or random diffusion processes. This is complicated even further by the fact that these effects may be dominant at different fields or temperatures or (partially) compensate each other. As such, there is no one given formula that is perfectly valid for all cases. In this paper, we have, therefore, decided to restrict our analysis to using only the simple model described by Eq. (1). This approach has some benefits as it provides us with two simple parameters, the trap depth and trap concentration, that can easily be linked to other experimental and computational observations and compared between samples. Moreover, a simple model avoids the real danger of overfitting the experimental data. While some deviations are to be expected, the interpretation of these deviations can, in turn, provide further insights. The choice of exponent for the electric field E in the pre-exponential part of Eq. (1) has no effect on the experimental extracted values of β nor ϕ but can influence the interpretation of the values obtained for N_c. However, as the samples are studied at similar electric fields, this does not pose a concern when focusing on relative trends.

Besides the Poole–Frenkel effect, other trap-assisted conduction mechanisms have been postulated. In the case of hopping conduction, rather than being excited to the conduction band, charge transport happens by direct hopping between neighboring localized states.[13] This type of transport is more likely to occur for materials where the distance between traps is small. In the case of hopping conduction, the current density and electric field are related according to the formula:[22] $J = qanv \cdot \exp\left(\frac{qaE}{kT} - \frac{E_a}{kt}\right)$. In this model, the most important parameters are the mean distance between traps a, the electron concentration in the conduction band n, the frequency of the thermal vibrations of electrons at the trap sites v and E_a, and the activation energy. Note how in contrast to Eq. (1), J is $\propto \exp(E)$. However, for most of the samples measured in this study we have found that $J \propto \exp(E^{1/2})$ fits the observed relationship better. Second, unlike with the simple Poole–Frenkel mechanism, the main parameters in the case of hopping conduction are less easily linked to other experimental results. For these reasons and the reasons mentioned earlier, we have restricted this study to the simple Poole–Frenkel model only.

III. EXPERIMENTAL

The films are deposited through sputter deposition using a $GeSe_2$ stoichiometric target, with additional Ge added via

16 July 2026 09:01:14

© Author(s) 2025

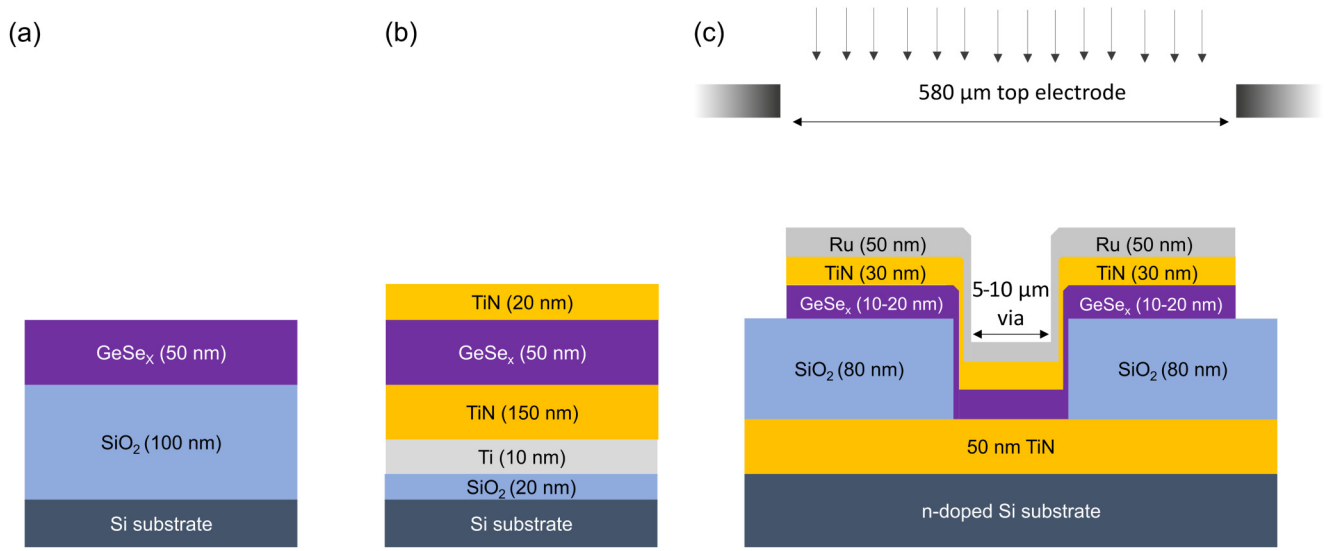

FIG. 2. (a) Schematic representation of the sample used for Raman analysis, (b) XRD and AFM analysis, and (c) electrical characterization.

co-sputtering from a Ge target in the case of the GeSe films. The film thickness is checked using x-ray reflectivity (XRR) and the composition of the films was verified using a combination of Rutherford backscattering spectrometry (RBS) and energy-dispersive x-ray spectroscopy (EDX) analysis. In Fig. 2, an overview is given of the sample structures used for the different analysis techniques. For Raman analysis, a 50 nm layer is deposited on top of a substrate consisting of 100 nm SiO_2 on Si as illustrated in Fig. 2(a). In the case of x-ray diffraction (XRD) and atomic force microscopy (AFM) analysis, the functional layer is sandwiched between TiN layers to avoid substrate interaction and sublimation during heating [Fig. 2(b)]. For electrical analysis, simple test structures, shown in Fig. 2(c), are fabricated using a pre-patterned substrate. This substrate consists of an 80 nm SiO_2 layer on top of a 50 nm TiN bottom electrode layer, deposited onto highly doped N-type Si. A grid of vias of 5 and 10 μm in diameter was etched into the SiO_2 layer. Subsequently, a shadow mask with 600 μm holes is aligned on top of the substrate and the functional $GeSe_x$ and TiN top electrode layers are sputtered through the shadow mask onto the substrate. This approach results in a sample with 28 easily measurable cells of a given size with a large top surface but a small bottom electrode of only a few micrometers in diameter. This structure is useful for quickly testing multiple compositions and gives good results when focusing on relative effects, but does not have some of the features of more complex test structures such as built-in series resistor to limit operating current. The layer thickness for electrical characterization is 10 or 20 nm.

The amorphous nature of the as-deposited layers is checked using XRD. Additionally, the crystallization temperature of the layers can be determined using an *in situ* approach. During the *in situ* XRD measurement, the samples are heated at a rate of 0.2 °C/s to 600 °C, under an inert atmosphere, while a fixed linear detector monitors a 2θ-window of 20°. Sample roughness was checked using a Bruker Dimension Edge AFM. Raman analysis was performed with a Horiba Jobin–Yvon LabRAM HR and a 9 mW 532 nm laser focused to a 1 μm spot size with 10% ND transmission filter. A detailed analysis of the Raman measurement approach can be found in a previous publication.[10]

Electrical characterization is performed using a Keithley 2601 SMU for slow quasi-static current–voltage (IV) sweeps and a Keysight 81150A pulse generator in combination with a MSOX3104T mixed oscilloscope for μs pulsed IV measurements. During electrical measurements, a positive voltage is applied to the top electrode while the backside of the sample is grounded. First, DC IV sweeps are performed using a mapping IV stage on a set of cells of each sample to determine the typical OTS selector statistics such as the pristine leakage current and the first-fire switching voltages at ambient temperatures. Second, all remaining pristine cells are tested for functionality using two repeated IV sweeps below the threshold voltage. These measurements are used to determine which cells are functional and can be used for further testing. On the cells which show normal and reproducible behavior, electrical characterization as a function of temperature is done on a home-built cryostat. Samples are placed on a small chuck inside a vacuum chamber. The chamber is pumped down to a base pressure in the range of 1×10^{-3} mbar to avoid excessive condensation and ice formation. The temperature of the chuck is regulated by the combination of a heater element and a liquid nitrogen cooling solution. The temperature is measured with a Pt100 probe clamped to the top of the chuck, right next to the sample. A PID controller automatically regulates the temperature by adjusting the heater's output power. Voltage is applied to individual cells on the top of the sample using a motorized probe inside the chamber. Using this tool, electrical measurements of the sample can be performed between temperatures of up to 373 K down to 113 K.

16 July 2026 09:01:14

© Author(s) 2025

IV. RESULTS AND DISCUSSION

A. Material characterization of as-deposited films

Prior to the deposition of the samples for electrical characterization, separate samples were prepared for process and material characterization. Two compositions were aimed for: $GeSe_2$ and GeSe. The latter composition will be referred to as Ge-rich due to the fact that this composition contains excess Ge compared to what would be needed for all atoms in the material to satisfy their valence requirements, i.e., achieve a completely filled outer shell through shared electrons,[23] using solely Ge–Se bonds. Using RBS, the composition of calibration samples was determined to be 33.5 at.% Ge for the $GeSe_2$ sample and 49.8 at.% Ge for the GeSe sample. These samples were then used to calibrate EDX, and during subsequent depositions, the composition of each sample was verified to be within 1 at.% of the targeted composition. Figure 3 contains the results of the XRD. The layers are amorphous as-deposited, as the *ex situ* XRD pattern in Fig. 3(c) only contains peaks that are also found in the substrate material, namely, those of face-centered TiN and hexagonal Ti. Figures 3(a) and 3(b) show the *in situ* XRD data of the as-deposited $GeSe_2$ and GeSe layers, respectively. At room temperature, no peaks are visible as the layers are amorphous prior to the heat treatment. As the temperature is increased, XRD peaks related to the material's orthorhombic crystalline phase first appear at 530 °C for $GeSe_2$ and 358 °C for GeSe.[24,25] These crystallization temperatures are in line with those previously reported.[10,28] In Fig. 4, the AFM results of the as-deposited layers are shown. The layers are uniform and smooth, with an average RMS roughness of 1.4 nm for $GeSe_2$ and 1.1 nm for GeSe.

The results of the Raman analysis are shown in Fig. 5. The $GeSe_2$ spectrum is dominated by the peaks associated with heteropolar bonds between corner- and edgeshared (CS/ES) $GeSe_4$ tetrahedra that make up the bulk of the amorphous matrix. Other peaks include the shoulder peak at 170 cm^{-1} associated with the stretching of Ge–Ge bonds in Ge_2Se_4 ethane-like structures (ETH) as well as modes related to Se–Se chains and amorphous Ge–Ge bonds. These homopolar bonds are sometimes referred to as "wrong" bonds,[23,29,30] and their presence is a primary source of defect related trap states in the mobility gap of the material.[11,29,31] In the spectrum of the GeSe film, the overall intensity of the Raman signal is lower due to increased absorption of the probing laser. Nevertheless, the intensity of the peaks related to Ge–Ge wrong bonds, both the ethane-like and amorphous-like, is far greater compared to those related to Ge–Se bonds, implying a more numerous presence of these types of defects.

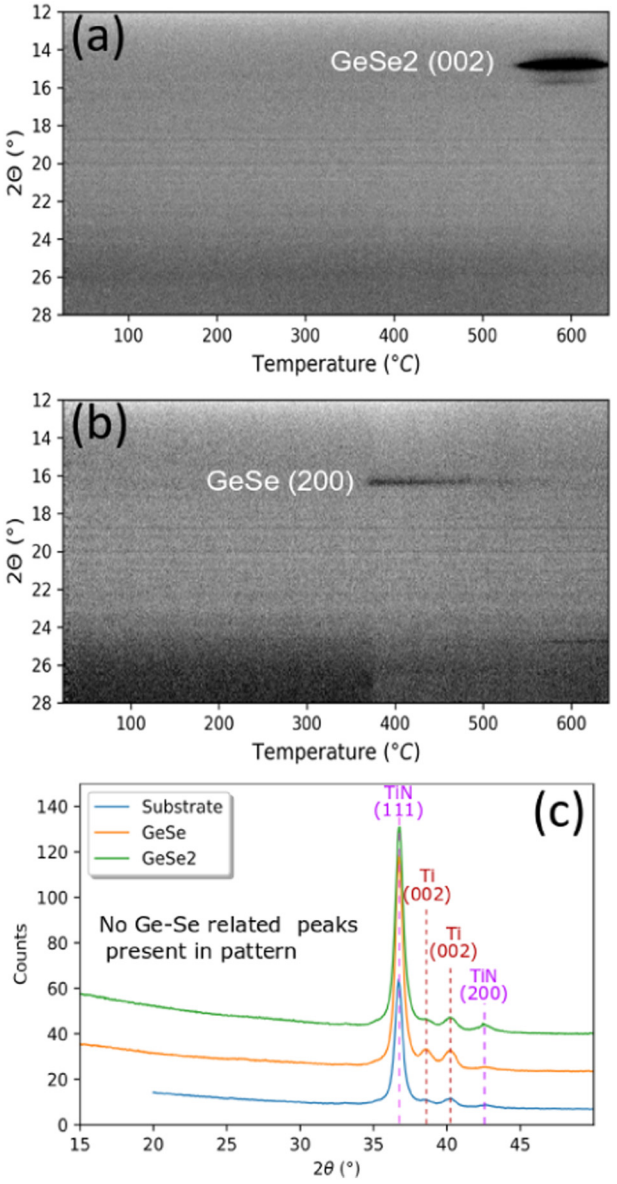

FIG. 3. (a) *In situ* XRD pattern of as-deposited $GeSe_2$ layer. (b) *In situ* XRD pattern of as-deposited GeSe layer. (c) *Ex situ* XRD scan of both layers as well as the substrate used for XRD analysis. Relevant peaks have been indicated.[24–27]

B. Electrical characterization in ambient conditions

The purpose of the ambient electrical characterization is two-fold. First, it is used to extract some typical OTS selector parameters such as the pristine leakage and the first-fire switching voltage. The latter is particularly important as during the temperature controlled analysis, the cells must only be measured in the sub-threshold regime. Thus, the ambient first-fire analysis helps establish the maximum voltage that may be applied during the temperature controlled analysis. Second, ambient voltage sweeps are also used to screen all cells on a given sample to check their functionality. For practical reasons, it is not possible to measure the behavior of each cell as a function of temperature so a pre-screening is done in the sub-threshold regime to eliminate leaky cells. Two types of IV sweeps are performed: quasi-static DC voltage sweeps and μs scale pulsed measurements. An example of both types of measurements, showing the threshold switching of a

16 July 2026 09:01:14

© Author(s) 2025

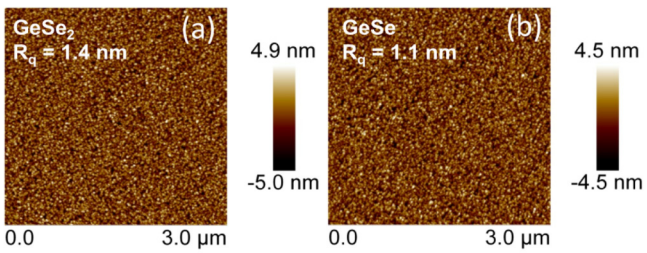

FIG. 4. (a) AFM image of $GeSe_2$ film. (b) AFM image of GeSe film.

20 nm GeSe layer, is shown in Fig. 6. As the quasi-static DC sweeps put considerable stress on the cells, they will often exhibit a persistent switch in resistance. In order to achieve volatile switching, short pulses are applied instead. Additionally, the current is limited with an external 2.2 kΩ series resistor. Using pulsed measurement, the impact of cycling the cell multiple times on the sub-threshold conduction can be studied.

The results of the ambient characterization are summarized in Fig. 7 in the form of boxplots. In Fig. 7(a), the first-fire threshold voltages are shown, separated by via size, layer thickness, and material. There is no clear dependence on via size, though the smaller via sizes seem to exhibit slightly less spread. In the case of 10 nm $GeSe_2$, V_{FF} is roughly halve that of a 20 nm film. This is not surprising as achieving the same critical electric field in a halve as thick layer will require a voltage halve as high, assuming the field is uniform. Interestingly, however, for GeSe, the required voltage is not halve as large. This may indicate that the electric field inside the layer is less uniform or alternatively that the switching is determined more heavily by interface effects for the 10 nm GeSe layer than it is for $GeSe_2$. Comparing the V_{FF} of $GeSe_2$ to that of GeSe,

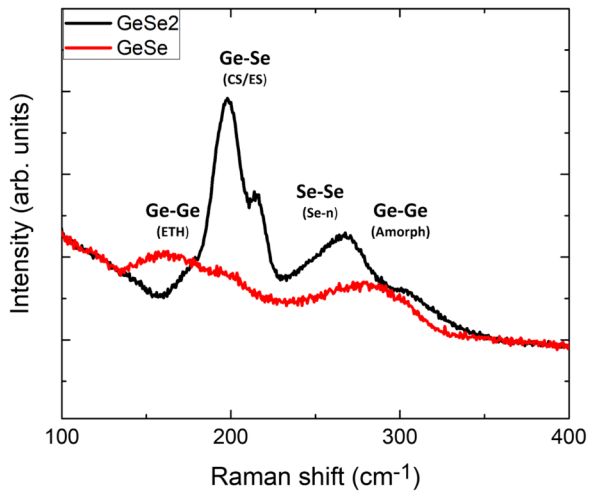

FIG. 5. Raman spectrum of as-deposited $GeSe_2$ and GeSe films. The regions where the most important peaks appear have been marked.[32–37]

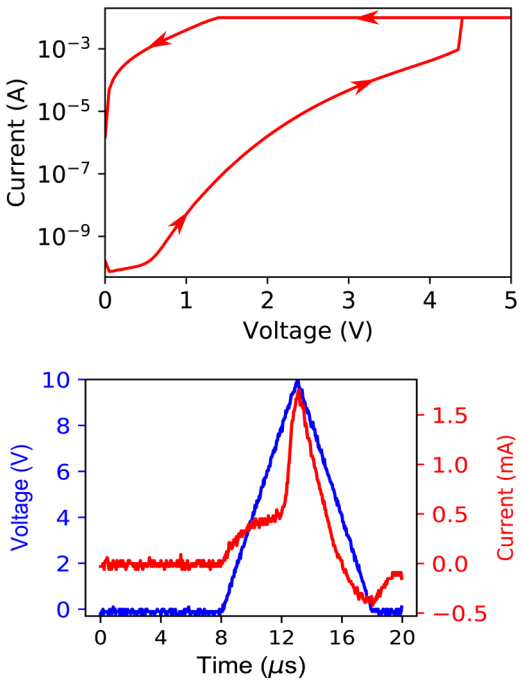

FIG. 6. Top: example of a quasi-static DC IV voltage sweep of a 20 nm GeSe film. The arrows denote the direction of the voltage sweep. Bottom: example of a pulsed IV measurement of a 20 nm GeSe film.

in case of the thicker layers, there is a decrease in the voltage for the Ge richer layers in line with expectations based on the bulk properties of $GeSe_x$ such as the bandgap, which is lower for GeSe than for $GeSe_2$.[38] In case of the thinner films, this dependence is not observed, indicating again that other effects may become more dominant, such as the interface with the electrode material as the material becomes thinner. For both materials, the results reflect those previously obtained on similar layers as part of a separate study.[9,10] The pristine leakage current was determined at 2 V and can be found in Figs. 7(b) and 7(c) for $GeSe_2$ and GeSe, respectively. To account for the two via sizes, the current density is plotted instead. With the exception of a few outliers, the spread in the data is relatively small. As expected, thicker layers exhibit lower leakage current. As the Ge content is increased, the leakage current drastically increases, in agreement with trends found in the literature and previously obtained results.[9,10] Finally, in Figs. 7(d) and 7(e), the leakage currents of, respectively, 10 nm $GeSe_2$ and 20 nm GeSe pristine cells are compared to those of cells that have been cycled a few times with a short voltage pulse. Unfortunately, no complete dataset could be obtained for the 20 nm $GeSe_2$ cells, nor the 10 nm GeSe cells as these would often either not switch to, or remain stuck in, the low resistive state, respectively. As such, figures (d) and (e) are only meant to demonstrate the impact of switching on the leakage current but not the impact of material or thickness, for which we refer to figures (c) and (d). As the switching voltage of cycled cells is lower, the sub threshold current at 1 V

16 July 2026 09:01:14

© Author(s) 2025

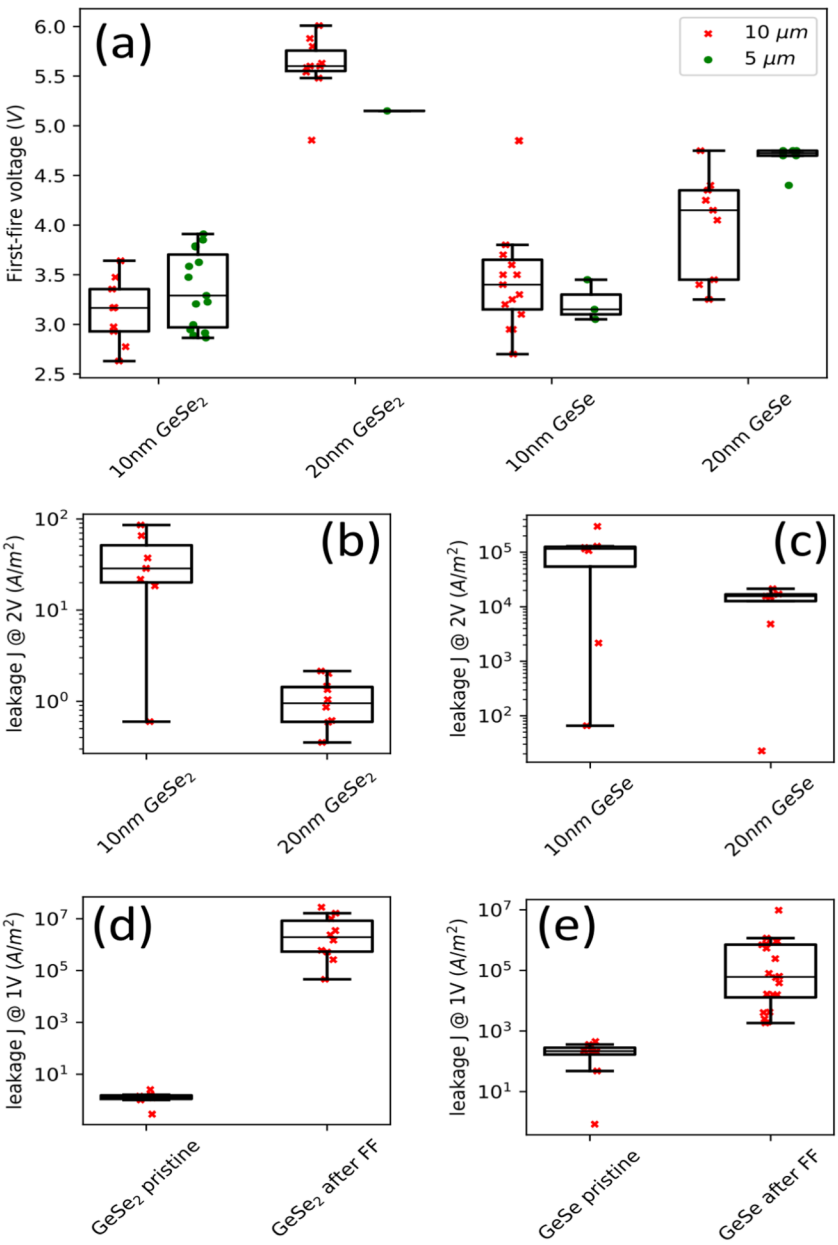

FIG. 7. (a) First-fire voltages determined using quasi-static DC voltage sweeps. The results are separated by size, material, and layer thickness. (b) Leakage current of pristine $GeSe_2$ cells at 2 V. (c) Leakage current of pristine GeSe cells at 2 V. (d) Comparison of the leakage current at 1 V for pristine and switched 10 nm $GeSe_2$ cells. (e) Comparison of the leakage current at 1 V for pristine and switched 20 nm GeSe cells.

is considered instead of at 2 V. The leakage of cycled cells is considerably larger and there is more spread due to the stochastic nature of the switching process. The increased leakage has previously been attributed to changes in the electronic or structural nature of the material after first-fire (FF). In the work by Kabuyanagi *et al.*,[39] the switching process is described using a percolation cluster model. Under the influence of the applied electric field, defects transition from a localized to a delocalized state until a critical field is reached. At this critical field, it is believed that a path of delocalized defects is formed that bridges both electrodes on either side of the chalcogenide. As the applied field is removed, delocalized-to-localized transitions take place, though some defects may remain in their delocalized state, and the number of remaining delocalized defects would then determine the leakage current. The switching speed, most often referring to the delay between the application of a voltage pulse exceeding the threshold voltage and the complete transition of the device from the HRS to the LRS, is another important ambient performance parameter. For GeSe-based OTS selectors, switching speeds below 10 ns are often reported.[3,40–42] The switching speed may also provide some insight into the switching

16 July 2026 09:01:14

© Author(s) 2025

mechanism as a purely electronic switching mechanism, such as OTS, will have a different switching speed than a process, which also involves a change in the crystalline phase of the material (such as observed in phase change memory).[43,44] The sample structure used throughout this study, however, was optimized for low-temperature measurements of the sub-threshold current. A notable downside of their design though is that the large surface area gives rise to a high capacitance and the resulting charge and discharge effects during pulsed IV measurement hinder accurate determinations of the switching speed. For this reason, the switching speed was not considered in this study.

C. Temperature controlled IV analysis

1. Typical behavior of pristine layers

During the temperature controlled IV(T) measurements, quasi-static DC IV sweeps are performed on a selection of reproducibly behaving cells of a given sample. The sweep rate is kept as low as possible at 0.05 V/s to increase measurement accuracy and reduce parasitic capacitance related effects, caused by the comparatively large surface area of the test samples, that can disrupt very low current measurements. The maximum applied voltage is determined by the first-fire voltage (V_{FF}) in Fig. 7 and kept below the lowest data point in the boxplot to ensure the cell remains in its pristine state throughout the temperature dependent analysis. In Fig. 8, a typical IV(T) measurement is depicted for the four combinations of composition and layer thickness, on cells with a via size of 5 μm. The typical temperature range stretches from 353 to 113 K. To further reduce the effects of noise and capacitive effects, what is plotted here is the average of the up and down parts of the triangular voltage sweep. A clear temperature dependence of the IV sweeps is visible and as the temperature decrease, the overall current through the cell decreases. At low temperatures and voltages, this can result in the current dropping below the noise level of the measurement tool, which limits the range in which the behavior can be studied. To check the validity of the PF model, IV sweeps are often replotted as a Poole–Frenkel plot. In a PF plot, the natural logarithm of the current density divided by the electric field is plotted as a function of the square root of the electric field. If the conduction can be described by the PF equation [see Eq. (1)], the plot should result in a straight line.[45,46]

The PF plots of the same data used for Fig. 8 are shown in Fig. 9. For sufficiently high electric fields, the curves are straight, implying that PF conduction is valid in this regime. At lower electric fields, there are clear deviations, particularly for the $GeSe_2$ films. At these fields, the dependence between J and E is better described by $J \propto \exp(\sqrt{E})$ instead of $J \propto E \cdot \exp(\sqrt{E})$. This difference in the pre-exponential factor has been reported before[16] and can be related to phenomena such as re-trapping of excited charge carriers. Such a dependency, however, predicts non-zero current at zero field and can thus only be an approximation. Alternatively, it could indicate that at low voltages or currents, the behavior of cells does not follow PF conduction anymore and is dominated by other effects. A full analysis of low field behavior is beyond the scope of this paper though as only for a limited temperature range does the current exceed the detection limit of the tool. Instead, the analysis is restricted to ranges in which the equation for PF conduction is satisfied. Indicated on the figure are the ranges to which the temperature dependent analysis was restricted.

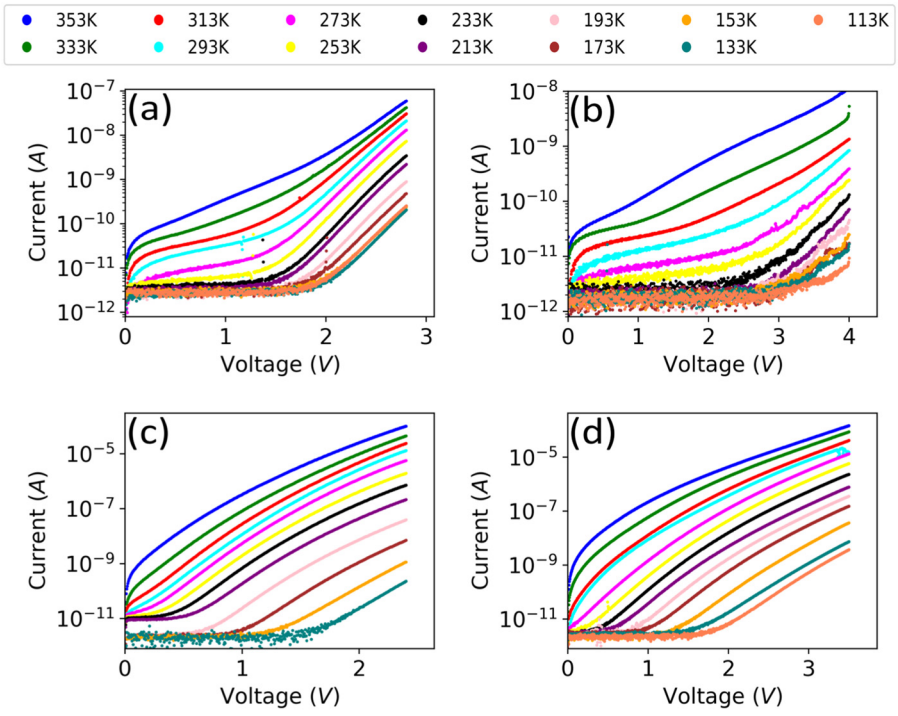

FIG. 8. Typical temperature controlled IV measurement for a layer of (a) 10 nm $GeSe_2$, (b) 20 nm $GeSe_2$, (c) 10 nm GeSe, and (d) 20 nm GeSe. For each example, the via size was 5 μm.

16 July 2026 09:01:14

© Author(s) 2025

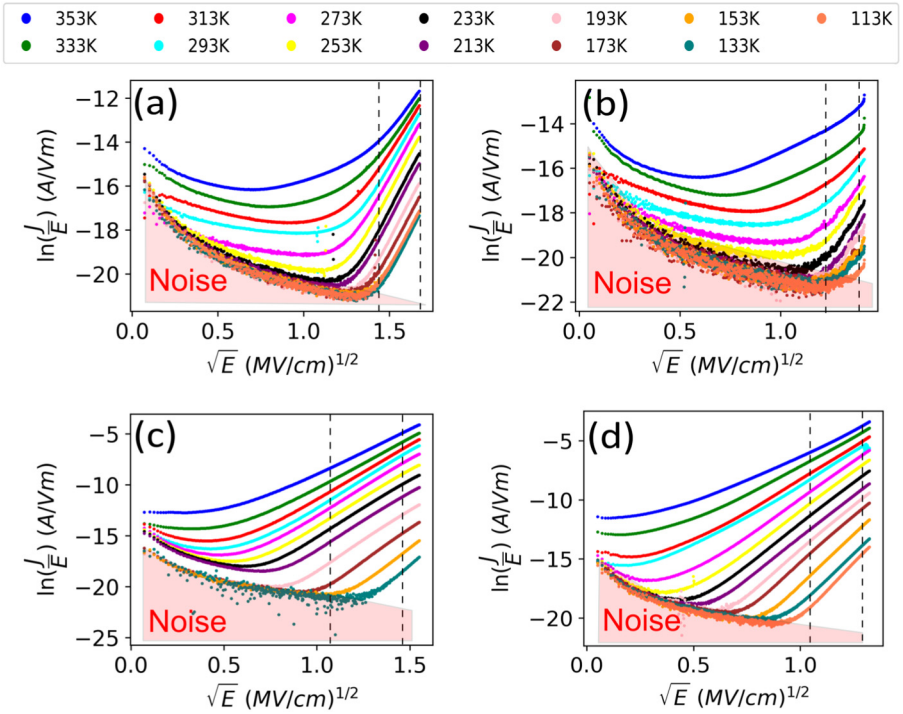

FIG. 9. PF plot for a layer of (a) 10 nm $GeSe_2$, (b) 20 nm $GeSe_2$, (c) 10 nm GeSe, and (d) 20 nm GeSe. For each example, the via size was 5 μm. The dotted lines indicate the range in which the temperature dependent behavior was studied and the red shaded area indicates roughly the noise limit of the measurement tool.

Equation (1) can be re-written in the following way:

$$\ln(J/E) = \ln(q\mu N_c) - \frac{q\phi - \beta\sqrt{E}}{kT}. \quad (2)$$

When plotting ln(J/E) as a function of 1/T for various voltages and fitting a linear behavior, the reduced barrier height can be obtained by looking at the slope of each line. The trap depth can then be found by extrapolating to zero electric field. The intersect of each line in the ln(J/E)−1/T plot with the y-axis is equal to the first part of Eq. (2), which is proportional to the density of traps within the mobility gap. An example of this analysis for a 20 nm GeSe layer is shown in Fig. 10. A first thing to notice is that the ln(J/E) vs 1/T curves are not perfectly straight across the full temperature range, rather the slope becomes less steep at lower temperatures. This suggests a changing barrier height with respect to temperature. When restricting the temperature range to a high T (353–293 K), medium T (313–213 K), and low T regime (233–173 K), a good linear fit can still be achieved for each temperature range. These ranges were selected because they result in good fits for all samples. At even lower temperatures, the current approaches the measurement limit for certain samples, and therefore the lowest temperature data points (below 173 K) are not used for the analysis. When plotting the slope of each temperature regime as a function of $\sqrt{E}$ and extrapolating to zero field, three different values for the trap depth are obtained. This suggests that the mobility gap of the material contains a distribution of traps centered around different energy levels as opposed to only one energy level. Indeed, simulations from first principles on similar $GeSe_x$ layers suggest the presence of different types of localized states.[11] At higher temperatures, deep traps can contribute to the conduction and a resulting trap depth of around 0.64 eV is found. At the lowest temperatures, only the most shallow traps can contribute and the extracted trap depth is consequently lower, at 0.28 eV. The medium range gives an in-between value of 0.48 eV. The slope of the plots in the bottom figure also contains valuable information. This slope is equal to the Poole–Frenkel constant $\beta_{PF} = \sqrt{\frac{q^3}{\pi\epsilon_0\epsilon_r}}$ and should only depend on the relative dielectric constant of the material. In the case of 20 nm GeSe, we see that the slopes extracted for different temperature regimes are relatively constant. Some variations are to be expected as a slight temperature dependence of the dielectric constant is expected. In the case of 20 nm GeSe, the slope for the high temperature regime results in a value for β_{PF} of $2.9 \times 10^{-5}\, e\sqrt{Vm}$ (with e being the elementary charge). This value is in good agreement with the expected value for RF sputtered deposited GeSe thin films based on a relative dielectric constant ϵ_r of 7 reported in several studies.[47,48] It should be noted though that other, more recent papers report a higher value of ϵ_r, which would result in a lower expected value of β_{PF}.[49,50]

In Fig. 11, the PF analysis is shown for the four combinations of layer thickness and composition. For the ln(J/E) vs 1/T plots, the medium range fit has been extrapolated to also show the intercept with the y-axis. This value corresponds to the first part of Eq. (2), $\ln(q\mu N_c)$ and is proportional to the density of trap states. In the ideal PF model, the intercept should be the same for every voltage; in practice, this does not appear to be the case. In the work by

16 July 2026 09:01:14

© Author(s) 2025

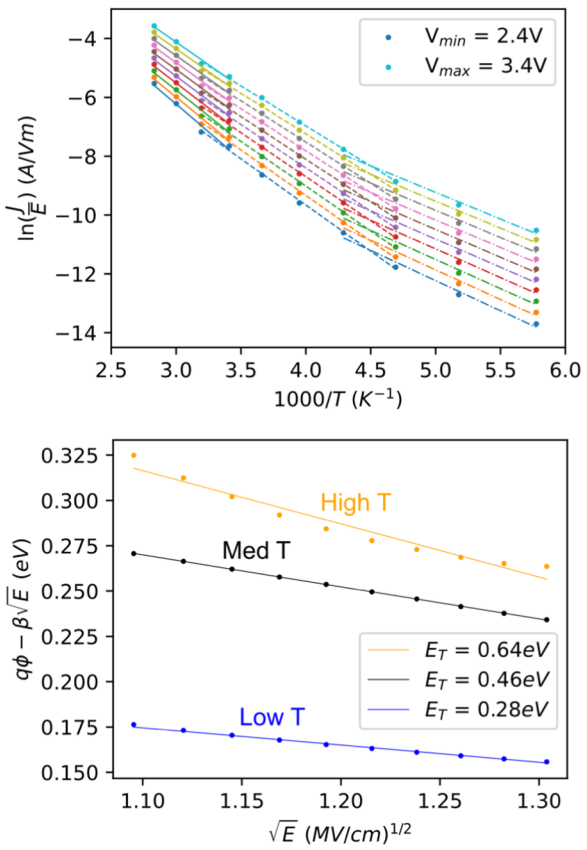

FIG. 10. Example of the PF analysis for a 20 nm GeSe layer. The temperature range was divided into three distinct ranges: a high T range, a medium T range, and a low T range. The top figure shows the J/E vs 1/T at various voltages. In the bottom figure, the slopes of the fitted lines are plotted as a function of $\sqrt{E}$. Extrapolating to zero field gives the trap depth shown in the legend.

Clima *et al.*,[11] it is shown that the electric field can influence the density of states, which may partially explain the shift in intercept value. The model also assumes a field independent mobility factor, which may not be valid for all fields. It should be noted that the applied electric field for all the samples is roughly the same though and lies between 1.2 and 2.4 MV/cm. Significant differences (factor of 10^3–10^4) in the intercept value are observed between $GeSe_2$ layers as compared to the GeSe layers. Such differences would be difficult to explain with merely a difference in mobility factor so suggest a larger density of traps for the GeSe films as opposed to the $GeSe_2$ films. As evidenced by the Raman results, the Ge-rich layer hosts considerably more Ge–Ge related bonds. These additional Ge–Ge bonds give rise to additional gap states,[11] which explains the higher trap density. When comparing the trap depths between materials, the average trap depth in $GeSe_2$ layers appears to be deeper than that of GeSe layers. This may be explained by a difference in dominant trap type. Indeed, for Se-rich layers, the dominant trap type is reported to be Se lone-pair electrons,[11] located close to the valence band, with some additional contributions from over- or undercoordinated Ge atoms near the conduction band. This is in line with the Raman analysis showing a much larger abundance of Se–Se chains.

When looking at the slope of the trap depth analysis, an interesting observation can be made when comparing layers of different thickness. There is less variation in slope between the temperature ranges for the thicker layers for both GeSe and $GeSe_2$, consistent with the simple PF model, which predicts a constant slope in the case of a temperature independent ϵ_r. Additionally, when comparing the 20 nm films to the 10 nm films for a given composition, the slopes of the high temperature regime are similar while the slopes differ more at lower temperatures. These observations suggest that for thicker films, and at higher temperatures, PF conduction as predicted by the simple model is valid, when allowing for multiple trap levels. For thinner films and at lower temperatures however, there are more deviations from the predicted PF behavior. A likely explanation lies in the fact that the simple PF model concerns itself only with the conduction through the bulk of the layer, which is assumed to be the current limiting factor. For thinner films, especially at lower temperatures, this may not be the case and charge transport across the interface barriers may start to dominate. In the case of current limitation due to Schottky emission at the interfaces, for instance, the expected slopes would be lower since the barrier lowering factor $\beta_{schottky} = \beta_{PF}/2$. As such, the less steep slope for the thinner films at lower temperature may be an indication that Schottky emission is current limiting over PF conduction. The results shown in Fig. 11 are those of typical samples. The above analysis was performed on several cells of each sample. In Fig. 14, the data of multiple cells are combined and the same observations hold true.

2. Switched layers

Besides the analysis of pristine layers, the IV(T) behavior of layers that have undergone first-fire has been studied. However, there are additional concerns when applying the simple PF model to the IV(T) data of switched layers. Previous studies have shown that after first-fire, the current may no longer scale with the area of the device,[51] indicating a more filamentary behavior. According to the percolation model[39] of the first-fire switching, this can be attributed to the presence of some amount of residual delocalized traps within the material that form a preferential current path. As a result, the real effective current density will always be higher than that obtained by dividing the current by the surface area of the device. This is illustrated in Fig. 12. The trap depth, however, is not affected by the change in the area parameter. Despite these shortcomings, it may still be interesting to look at what happens if we apply the simple PF model to IV(T) data of switched devices, naively calculating the current density by dividing the measured current by the area of the device. For this purpose, only the 10 nm $GeSe_2$ and the 20 nm GeSe layers were selected as these exhibited the most reliable switching behavior after first-fire.

In Fig. 13, the PF analysis of a typical switched 10 nm $GeSe_2$ and switched 20 nm GeSe layer is shown. For these cycled devices, it may sometimes occur that the device exhibits a recovery effect where during an IV sweep below the threshold voltage an increase in cell resistance is observed. This is attributed to the partial

16 July 2026 09:01:14

© Author(s) 2025

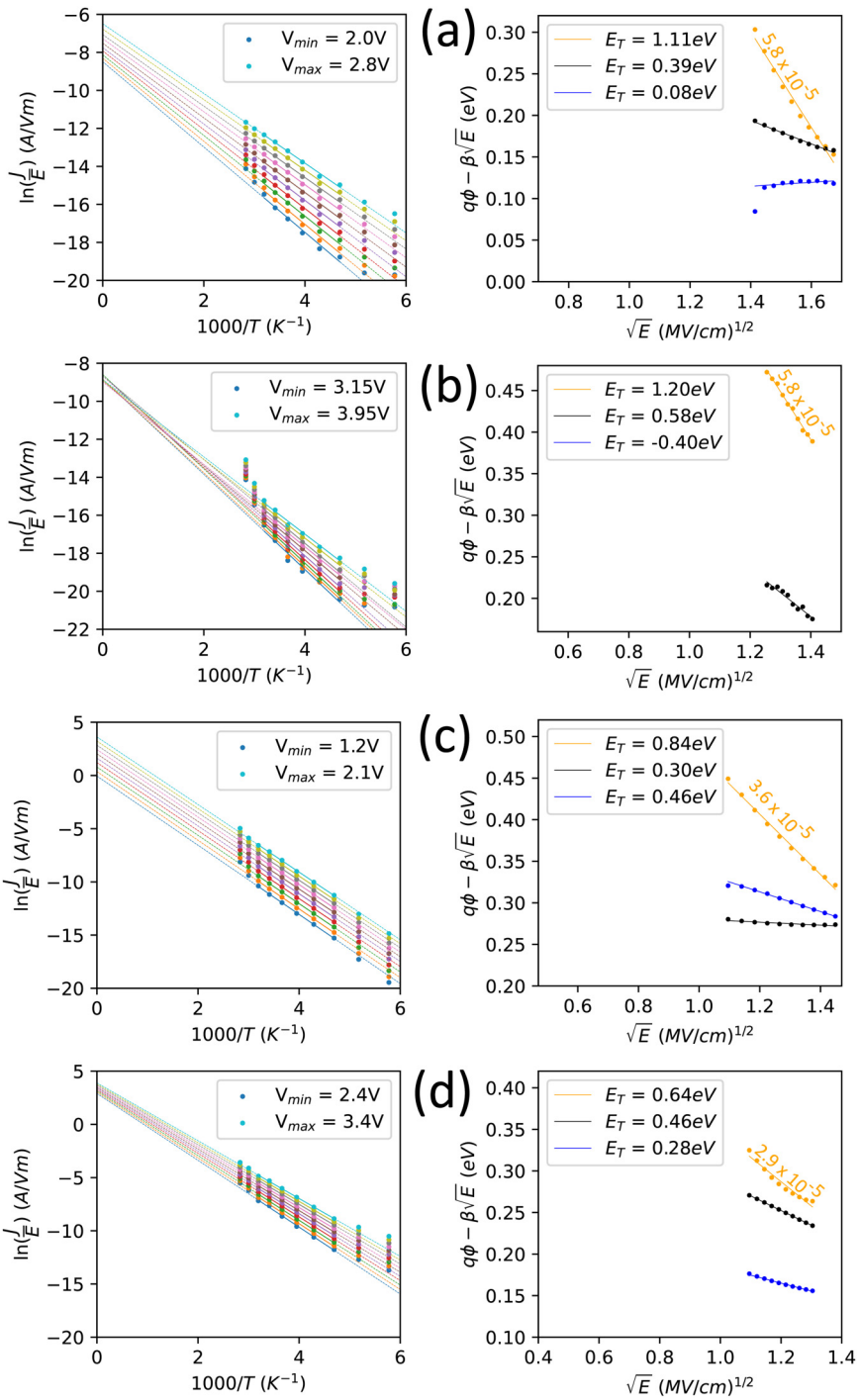

FIG. 11. Comparison of the PF analysis of typical pristine layers for the various combinations of thickness and composition: (a) 10 nm $GeSe_2$, (b) 20 nm $GeSe_2$, (c) 10 nm GeSe, and (d) 20 nm GeSe. In the J/E vs 1/T plots, the full line represents the medium temperature fitting regime and the dotted lines are extrapolations. The Poole–Frenkel factor β_{pf} (in units of $e\sqrt{Vm}$) for the high temperature regime has been noted on each plot of the trap depth.

relaxation of some de-localized trap states left over from the switching event. Usually, after a one or two sweeps, the cell will have fully relaxed but this can cause a step in the J/E vs 1/T plot, particularly around the 293 and 273 K data points because those are the temperatures that are measured first. For this reason, slightly different temperature ranges have been chosen and the medium temperature range was omitted. Instead, a high temperature range from 353 to 313 K and a low temperature range of 253 to 173 K is used. Within the selected ranges, there is good agreement between the fit and the data. Instantly noticeable is the much lower trap depth for both

16 July 2026 09:01:14

© Author(s) 2025

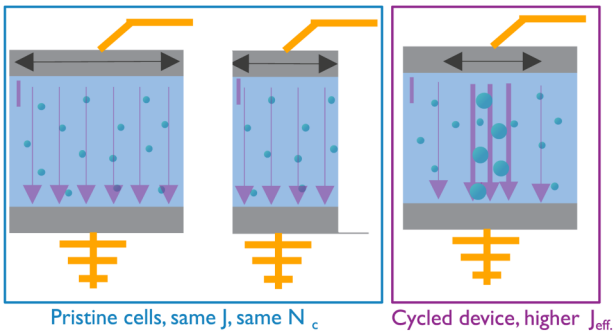

FIG. 12. Illustration of how filamentary conduction can result in a larger effective current density.

$GeSe_2$ and GeSe switched samples compared to their pristine counterparts, which suggest a significant change in the electronic structure of the devices after first-fire. It should be noted that the trap depth parameter does not depend on the surface area of the device. For both materials, the slope of the trap depth analysis plot does not vary significantly between the two temperature ranges, implying the dominant conduction mechanisms do not change as the temperature changes. Compared to the pristine case, the slopes have decreased significantly though, which may indicate a change in the dominant conduction mechanism or dielectric constant of the material on which the slope depends. The obtained trap depth is once again temperature dependent, corresponding to a distribution of trap depths, though to a much smaller degree than is the case for pristine layers, which may indicate a narrower distribution of current-contributing trap state. The mean value for the intercept with the y axis is −2.2 A/Vm for the high T range in the case of $GeSe_2$ and similarly −2.0 A/Vm for GeSe layers. This represents a slight increase for $GeSe_2$ and a significant decrease in the case of GeSe. As mentioned before, this value is proportional to the electron mobility and the density of trap states.

The findings regarding the change in trap depth after first-fire can support the percolation model of the first-fire switching. Within our application of the simple PF model, the presence of residual delocalized trap states may reflect itself in a significant decrease in the average trap depth. Interpretation of the density of traps is more difficult. Since this parameter is extracted from the pre-exponential factor, it is directly tied to the current density via the area of the device. As stated above, since the effective area through which conduction occurs will be lower than the area of the device, there will be an underestimation of the effective current density and, consequently, the trap density.

D. Analysis of multiple cells

The above discussion was based on typical example cells. Multiple cells were measured on each sample. In Fig. 14, the data of all these cells have been combined to show the average trap depth and trap density for each sample. Error bars indicating the standard error have been added to show the spread of the data. This representation illustrates a clear separation between $GeSe_2$ and GeSe layers in their pristine state. As before, the high temperature

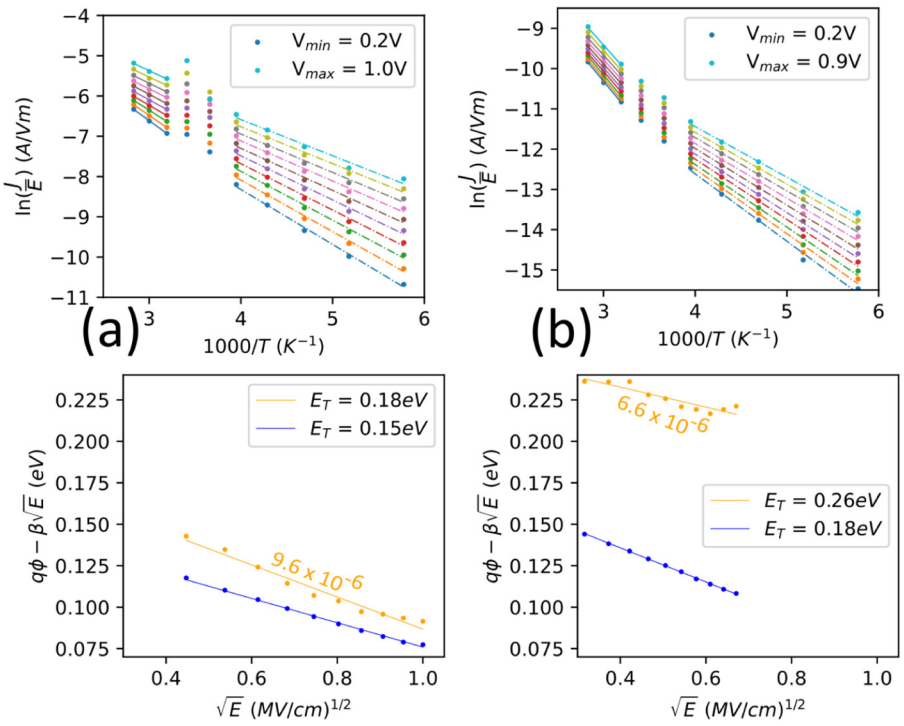

FIG. 13. PF analysis of switched 10 nm $GeSe_2$ (a) and 20 nm GeSe (b). The temperature ranges have been adjusted to avoid the regime where additional relaxation may take place, as evident by the behavior seen in figure (a) around the 293 and 273 K points. B_{PF} for the high temperature regimes are indicated in the trap depth analysis. The current density was calculated by dividing the measurement current by the total device area.

16 July 2026 09:01:14

© Author(s) 2025

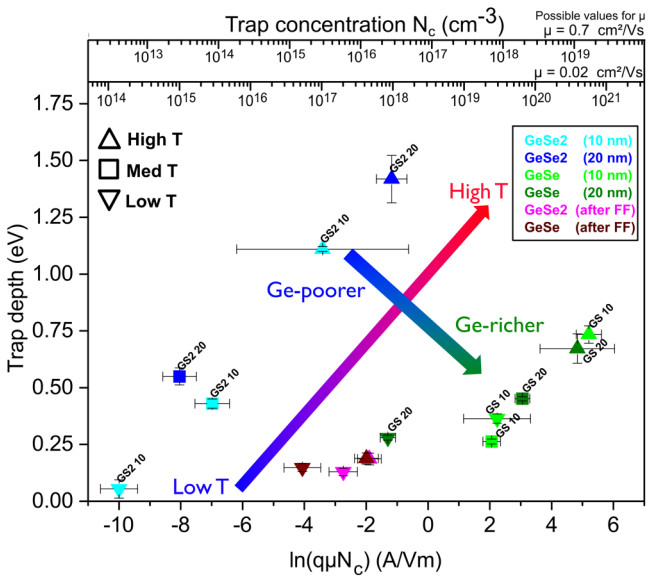

FIG. 14. Overview of the PF parameters mean trap depth and mean trap concentration obtained from multiple cells per sample. The colors denote the various samples. The temperature range is indicated by the shape of the data. The bottom axis represents the intercept parameter of Eq. (2). By substituting in the elemental charge and reasonable estimates for the mobility μ,[52,53] a value for the effective trap density N_c can be read from the top horizontal axes. The error bars indicate the standard error defined as $\frac{\sigma}{\sqrt{n}}$. In the case of GS_2 10, the error in trap concentration is somewhat inflated due to the presence of an outlier.

measurements result in the highest trap depths and vice versa. There is an apparent relation between the obtained trap depth and the estimated density of traps. This is not surprising considering that at lower temperatures only the shallower traps can contribute to the current and hence will be detected by the analysis while at higher temperatures both shallow and deep traps can contribute, resulting in an on average higher trap depth and a higher effective trap concentration.

V. CONCLUSIONS

In this paper, we have combined material characterization and ambient IV measurements with temperature dependent IV measurements. By applying a simple PF model for the conduction mechanism, several correlations between the PF model parameters trap depth and concentration and the material characteristics and OTS performance can be observed. Considering first only the 20 nm samples studied at higher temperature, it is found that GeSe layers contain a significantly larger amount of trap states than $GeSe_2$ layers. In addition, the average depth of the distribution of the trap states is lower for GeSe than it is for $GeSe_2$. This is in line with DFT calculations published elsewhere and the Raman analysis included in this paper, which indicate a significantly larger presence of homopolar Ge–Ge bonds in GeSe compared to $GeSe_2$, which may act as a source of traps. In the latter, Se–Se bonds are present in greater number and give rise to deeper lying traps. The increased number of shallower traps for GeSe is also reflected in the ambient OTS parameters such as the pristine leakage and first-fire threshold voltage, which are, respectively, higher and lower than in the case of $GeSe_2$. Within a limited temperate range, the experimental data fit the simple PF model well but at lower temperatures, different values for trap depth are found. Within the model, this can be understood when allowing for several trap populations within the mobility gap instead of a single trap level.

When comparing the thinner 10 nm films, good linear fits are still obtained and the same correlations are found to be true but a detailed study of the temperature dependent IV curves reveals that for thinner films there are more deviations from the simple PF model. These deviations can be explained by the fact that for thinner films, particularly at lower temperatures, the leakage current may not be solely limited by conduction through the bulk but other mechanisms such as the charge carrier transport across interface barriers, by means of Schottky emission or tunneling, may play a large role.

After first-fire, the leakage current through the cell is significantly increased and the extracted trap depth is significantly lower, even when probing at elevated temperature. This suggests that the conduction is no longer governed by the same traps as in the pristine layers. The percolation model of first-fire switching predicts that after FF a certain amount of defect states remain in a delocalized state and conduction happens mostly through these defects. The presence of these defects could be considered analogous to a large amount of very shallow states in the sense that once a charge enters such a defect it is essentially free to move throughout the material. This might explain the apparent lower trap depth extracted from the PF model. However, it should also be noted that there is a significant difference in β_{PF} compared to the pristine layers. This suggests either that the dielectric constant has changed significantly or that there may be other conduction mechanisms and effects present that cannot be well described using just the simple PF model.

16 July 2026 09:01:14

ACKNOWLEDGMENTS

This research was made possible with the financial support of the BOF-UGent GOA-01G01019 project. Some of the materials required for the fabrication of test samples were provided by the Interuniversity Micro Electronics Center (IMEC). The authors would like to thank Stefanie Sergeant and Thomas Nuytten for their support with the Raman analysis.

AUTHOR DECLARATIONS

Conflict of Interest

The authors have no conflicts to disclose.

Author Contributions

Jonas Keukelier and Seppe van Dyck contributed equally to this work.

Jonas Keukelier: Formal analysis (equal); Resources (equal); Visualization (equal); Writing – original draft (lead); Writing – review & editing (lead). **Seppe Van Dyck:** Formal analysis (equal); Investigation (lead); Resources (equal); Visualization (equal).

© Author(s) 2025

Wouter Devulder: Conceptualization (lead); Resources (supporting); Writing – review & editing (equal). **Karl Opsomer:** Conceptualization (equal); Writing – review & editing (supporting). **Christophe Detavernier:** Conceptualization (equal); Project administration (lead); Writing – review & editing (equal).

DATA AVAILABILITY

The data that support the findings of this study are available from the corresponding author upon reasonable request.

REFERENCES

[1]G. W. Burr, R. S. Shenoy, K. Virwani, P. Narayanan, A. Padilla, B. Kurdi, and H. Hwang, "Access devices for 3D crosspoint memory," J. Vac. Sci. Technol., B **32**, 040802 (2014).

[2]X. Peng, R. Madler, P.-Y. Chen, and S. Yu, "Cross-point memory design challenges and survey of selector device characteristics," J. Comput. Electron. **16**, 1167–1174 (2017).

[3]M. Zhu, K. Ren, and Z. Song, "Ovonic threshold switching selectors for three-dimensional stackable phase-change memory," MRS Bull. **44**, 715–720 (2019).

[4]N. S. Avasarala, B. Govoreanu, K. Opsomer, W. Devulder, S. Clima, C. Detavernier, M. van der Veen, J. Van Houdt, M. Henys, L. Goux *et al.*, "Doped GeSe materials for selector applications," in *2017 47th European Solid-State Device Research Conference (ESSDERC)* (IEEE, 2017), pp. 168–171.

[5]A. Velea, K. Opsomer, W. Devulder, J. Dumortier, J. Fan, C. Detavernier, M. Jurczak, and B. Govoreanu, "Te-based chalcogenide materials for selector applications," Sci. Rep. **7**, 8103 (2017).

[6]J. Seo, S. W. Cho, H.-W. Ahn, B.-K. Cheong, and S. Lee, "A study on the interface between an amorphous chalcogenide and the electrode: Effect of the electrode on the characteristics of the ovonic threshold switch (OTS)," J. Alloys Compd. **691**, 880–883 (2017).

[7]V. Kumari, A. Kaswan, D. Patidar, K. Sharma, and N. Saxena, "Electrical conduction mechanism in GeSeSb chalcogenide glasses," Bull. Mater. Sci. **39**, 255–262 (2016).

[8]M. El-Samanoudy, "Modified Poole–Frenkel mechanisms in $Ge_{25+}Bi_xSb_{15-x}S_{60}$ thin films," Appl. Surf. Sci. **207**, 219–226 (2003).

[9]J. Keukelier, K. Opsomer, T. Nuytten, S. Sergeant, W. Devulder, S. Clima, L. Goux, G. S. Kar, and C. Detavernier, "Impact of changes in bond structure on ovonic threshold switching behaviour in $GeSe_2$," J. Mater. Chem. C **9**, 117–126 (2021).

[10]J. Keukelier, K. Opsomer, W. Devulder, S. Clima, L. Goux, G. Sankar Kar, and C. Detavernier, "Tuning of the thermal stability and ovonic threshold switching properties of GeSe with metallic and non-metallic alloying elements," J. Appl. Phys. **130**, 165103 (2021).

[11]S. Clima, D. Garbin, K. Opsomer, N. S. Avasarala, W. Devulder, I. Shlyakhov, J. Keukelier, G. L. Donadio, T. Witters, S. Kundu *et al.*, "Ovonic threshold-switching Ge_xSe_y chalcogenide materials: Stoichiometry, trap nature, and material relaxation from first principles," Phys. Status Solidi RRL **14**, 1900672 (2020).

[12]D. Ielmini and Y. Zhang, "Analytical model for subthreshold conduction and threshold switching in chalcogenide-based memory devices," J. Appl. Phys. **102**, 054517 (2007).

[13]D. Ielmini, "Threshold switching mechanism by high-field energy gain in the hopping transport of chalcogenide glasses," Phys. Rev. B **78**, 035308 (2008).

[14]J. Frenkel, "On pre-breakdown phenomena in insulators and electronic semiconductors," Phys. Rev. **54**, 647 (1938).

[15]J. Yeargan and H. Taylor, "The Poole-Frenkel effect with compensation present," J. Appl. Phys. **39**, 5600–5604 (1968).

[16]M. Boon, "The Poole-Frenkel pre-exponential factor," Thin Solid Films **11**, 183–185 (1972).

[17]R. M. Hill, "Poole-Frenkel conduction in amorphous solids," Philos. Mag. **23**, 59–86 (1971).

[18]Q. Pan and Q. Liu, "Poole–Frenkel emission saturation and its effects on time-to-failure in Ta-Ta_2O_5-MnO_2 capacitors," Adv. Mater. Sci. Eng. **2019**, 1–9 (2019).

[19]J. Hartke, "The three-dimensional Poole-Frenkel effect," J. Appl. Phys. **39**, 4871–4873 (1968).

[20]A. Jonscher, "Electronic properties of amorphous dielectric films," Thin Solid Films **1**, 213–234 (1967).

[21]R. Ongaro and A. Pillonnet, "Poole-Frenkel (PF) effect high field saturation," Rev. Phys. Appl. **24**, 1085–1095 (1989).

[22]F.-C. Chiu, C.-Y. Lee, and T.-M. Pan, "Current conduction mechanisms in Pr_2O_3/oxynitride laminated gate dielectrics," J. Appl. Phys. **105**, 074103 (2009).

[23]A. V. Kolobov and J. Tominaga, "Metastability and phase change phenomena," in *Chalcogenides* (Springer, Berlin, 2012).

[24]D. Grier, G. McCarthy, D. Seidler, and P. Boudjouk, ICDD Powder Diffraction File, No. 00-048-1226 (International Centre for Diffraction Data, 1993).

[25]G. Dittmar and H. Schäfer, "Die kristallstruktur von germaniumdiselenid," Acta Crystallogr., Sect. B **32**, 2726–2728 (1976).

[26]W. Wong-Ng, H. McMurdie, B. Paretzkin, C. Hubbard, and A. Dragoo, ICDD Powder Diffraction File, No. 00-038-1420 (International Centre for Diffraction Data, 1987).

[27]M. Jafari, M. Vaezzadeh, and S. Noroozizadeh, "Thermal stability of α phase of titanium by using X-ray diffraction," Metall. Mater. Trans. A **41**, 3287–3290 (2010).

[28]S.-D. Kim, H.-W. Ahn, S. yeol Shin, D. S. Jeong, S. H. Son, H. Lee, B.-K. Cheong, D. W. Shin, and S. Lee, "Effect of Ge concentration in Ge_xSe_{1-x} chalcogenide glass on the electronic structures and the characteristics of ovonic threshold switching (OTS) devices," ECS Solid State Lett. **2**, Q75 (2013).

[29]K. Tanaka, "Wrong bond in glasses: A comparative study on oxides and chalcogenides," J. Optoelectron. Adv. Mater. **4**, 505–512 (2002), available at https://old.joam.inoe.ro/arhiva/pdf4_3/Tanaka.pdf.

[30]T. Lee and S. Elliott, "Hypervalency in amorphous chalcogenides," Nat. Commun. **13**, 1458 (2022).

[31]S. Clima, B. Govoreanu, K. Opsomer, A. Velea, N. S. Avasarala, W. Devulder, I. Shlyakhov, G. L. Donadio, T. Witters, S. Kundu *et al.*, "Atomistic investigation of the electronic structure, thermal properties and conduction defects in Ge-rich Ge_xSe_{1-x} materials for selector applications," in *2017 IEEE International Electron Devices Meeting (IEDM)* (IEEE, 2017), pp. 4–1.

[32]R. Zhang, J. Ren, H. Jain, Y. Liu, Z. Xing, and G. Chen, "In-situ Raman spectroscopy study of photoinduced structural changes in Ge-rich chalcogenide films," J. Am. Ceram. Soc. **97**, 1421–1424 (2014).

[33]E. Baudet, C. Cardinaud, A. Girard, E. Rinnert, K. Michel, B. Bureau, and V. Nazabal, "Structural analysis of RF sputtered Ge-Sb-Se thin films by raman and X-ray photoelectron spectroscopies," J. Non-Cryst. Solids **444**, 64–72 (2016).

[34]Y.-L. Gan and L. Wang, "Analysis of raman spectra of GeAsSe glass using different peak-fitting method," Proc. SPIE **9446**, 94461V (2015).

[35]I. Chambouleyron and A. Zanatta, "Nitrogen in germanium," J. Appl. Phys. **84**, 1–30 (1998).

[36]K. Jackson, A. Briley, S. Grossman, D. V. Porezag, and M. R. Pederson, "Raman-active modes of a-$GeSe_2$ and a-GeS_2: A first-principles study," Phys. Rev. B **60**, R14985 (1999).

[37]M. Wihl, M. Cardona, and J. Tauc, "Raman scattering in amorphous Ge and III–V compounds," J. Non-Cryst. Solids **8–10**, 172–178 (1972).

[38]S. Clima, T. Ravsher, D. Garbin, R. Degraeve, A. Fantini, R. Delhougne, G. S. Kar, and G. Pourtois, "Ovonic threshold switch chalcogenides: Connecting the first-principles electronic structure to selector device parameters," ACS Appl. Electron. Mater. **5**, 461–469 (2022).

[39]S. Kabuyanagi, D. Garbin, A. Fantini, S. Clima, R. Degraeve, G. Donadio, W. Devulder, R. Delhougne, D. Cellier, A. Cockburn *et al.*, "Understanding of tunable selector performance in Si-Ge-As-Se OTS devices by extended percolation cluster model considering operation scheme and material design," in *2020 IEEE Symposium on VLSI Technology* (IEEE, 2020), pp. 1–2.

16 July 2026 09:01:14

© Author(s) 2025

[40]J. Zhao, Z. Zhao, Z. Song, and M. Zhu, "GeSe ovonic threshold switch: The impact of functional layer thickness and device size," Sci. Rep. **14**, 6685 (2024).
[41]M. Lee, S. Lee, M. Kim, J. Lee, C. Kwon, C. Won, T. Kim, S. Lee, S. Cho, S. Na *et al.*, "Ultrafast and thermally stable ternary Ge0.33SexSy ovonic threshold switching selector using magnetron sputtering," J. Alloys Compd. **973**, 172863 (2024).
[42]B. Govoreanu, G. L. Donadio, K. Opsomer, W. Devulder, V. Afanas' ev, T. Witters, S. Clima, N. S. Avasarala, A. Redolfi, S. Kundu *et al.*, "Thermally stable integrated Se-based ots selectors with >20 mA/cm^2 current drive, >3.10^3 half-bias nonlinearity, tunable threshold voltage and excellent endurance," in *2017 Symposium on VLSI Technology* (IEEE, 2017), pp. T92–T93.
[43]N. Saxena, R. Raghunathan, and A. Manivannan, "A scheme for enabling the ultimate speed of threshold switching in phase change memory devices," Sci. Rep. **11**, 6111 (2021).
[44]J. Shen, W. Song, K. Ren, Z. Song, P. Zhou, and M. Zhu, "Toward the speed limit of phase-change memory," Adv. Mater. **35**, 2208065 (2023).
[45]R. G. Southwick, J. Reed, C. Buu, R. Butler, G. Bersuker, and W. B. Knowlton, "Limitations of Poole-Frenkel conduction in bilayer HfO_2/SiO_2 MOS devices," IEEE Trans. Device Mater. Reliab. **10**, 201–207 (2009).
[46]H. Schroeder, "Poole-Frenkel-effect as dominating current mechanism in thin oxide films—An illusion?!" J. Appl. Phys. **117**, 215103 (2015).
[47]H. Hausler *et al.*, "Photoconductivity measurements on amorphous GeSe films," Phys. Stat. Solid. **40**, 15–17 (1977).
[48]C. Vodenicharov, S. Parvanov, and P. Petkov, "Electrode-limited currents in the thin-film m-GeSe-m system," Mater. Chem. Phys. **21**, 447–454 (1989).
[49]L. Guarneri, S. Jakobs, A. von Hoegen, S. Maier, M. Xu, M. Zhu, S. Wahl, C. Teichrib, Y. Zhou, O. Cojocaru-Mirédin *et al.*, "Metavalent bonding in crystalline solids: How does it collapse?" Adv. Mater. **33**, 2102356 (2021).
[50]S.-C. Liu, Y. Mi, D.-J. Xue, Y.-X. Chen, C. He, X. Liu, J.-S. Hu, and L.-J. Wan, "Investigation of physical and electronic properties of GeSe for photovoltaic applications," Adv. Electron. Mater. **3**, 1700141 (2017).
[51]Z. Chai, W. Zhang, R. Degraeve, S. Clima, F. Hatem, J. Zhang, P. Freitas, J. Marsland, A. Fantini, D. Garbin *et al.*, "Evidence of filamentary switching and relaxation mechanisms in Ge_xSe_{1-x} OTS selectors," in *2019 Symposium on VLSI Technology* (IEEE, 2019), pp. T238–T239.
[52]H. Li and J. Robertson, "Materials selection and mechanism of non-linear conduction in chalcogenide selector devices," Sci. Rep. **9**, 1867 (2019).
[53]G. I. Kim and J. Shirafuji, "Time of flight measurement of carrier mobility in Ge_xSe_{1-x} glasses," Jpn. J. Appl. Phys. **17**, 1789 (1978).

16 July 2026 09:01:14

© Author(s) 2025